

HIERARCHICALLY POROUS STRUCTURES FOR HIGH SURFACE AREA APPLICATIONS

A Thesis

Presented to the Faculty of the Graduate School

of Cornell University

in Partial Fulfillment of the Requirements for the Degree of

Master of Science

by

Thomas McCune

August 2016

© 2016 Thomas McCune

ABSTRACT

In this thesis, innovative nanoparticle synthesis approaches are implemented to produce porous structures that have high surface area and pore volume. In Part 1, sub-10 nm strontium titanate (SrTiO_3) particles were synthesized and templated with polystyrene nanoparticles (~50 nm) in conjunction with ice templation via a freeze-casting technique. The resulting materials show hierarchical structures consisting of organized 10-100 μm macropores and uniform 50 nm mesopores. In a photodegradation study, these hierarchical structures induced 100% degradation of rhodamine-B after only one hour of sunlight exposure. This hierarchically porous SrTiO_3 proves to be promising for increasing efficiency in photocatalysts.

In Part 2, mesoporous silica nanoparticles (MSNPs) of ~ 15 nm were synthesized and functionalized with pH-sensitive ligands in a one-pot synthesis procedure. After being loaded with dye, the MSNPs were shown to have pH-sensitive controlled release, pointing to their viability as drug delivery nano-carriers that are small enough to enter body cells via endocytosis.

BIOGRAPHICAL SKETCH

Thomas McCune is a Master of Science candidate in the department of Materials Science & Engineering at Cornell University. He also completed his Bachelor of Science degree in the same department, and has thoroughly enjoyed his rewarding five years of academics there. He is from Dix Hills, NY and aside from research his passions include skiing and tree climbing. Thomas plans to use the knowledge and experience gained from his years at Cornell to enter the field of semiconductor fabrication. He will be moving to Phoenix, Arizona at the conclusion of the summer of 2016 to work as a process engineer at Intel. He has aspirations of continuing research at the commercial level.

ACKNOWLEDGEMENTS

Emmanuel Giannelis provided support and advisement and generated the idea for the SrTiO₃ project. Genggeng Qi developed the design for synthesis recipes of SrTiO₃ and polystyrene latex nanoparticles. He also provided direct suggestions for the processes and experiment designs. Kai Ma developed the design for the synthesis of mesoporous silica nanoparticles. Previous Giannelis group members developed the ice templating procedure similar to the one used in this thesis. Members who made major contributions to the development of this procedure include Luis Estevez, Tiffany Williams, and Ritu Sahore. Cornell CNET and the Department of Materials Science & Engineering provided lab space and equipment.

TABLE OF CONTENTS

VOLUME 1

- I. Abstract
- II. Introduction
- III. Experimental
 - a. SrTiO₃ Synthesis
 - b. Polystyrene Latex Synthesis
 - c. Ice Templating
 - d. Heat Treatment and Sintering
 - e. Photodegradation of Rhodamine-B
- IV. Results
 - a. Nanoparticle Characterization
 - b. Pore Structure Characterization
 - c. Photodegradation Results
- V. References

VOLUME 2

- I. Abstract
- II. Introduction
- III. Experimental
 - a. Mesoporous Silica Nanoparticle (MSNP) Synthesis
 - b. Controlled Release Simulation Study
- IV. Results
 - a. Optimal Ligand Amount
 - b. MSNP Characterization
 - c. pH Response Verification
 - d. Controlled Release Results
- V. References

LIST OF FIGURES

VOLUME 1

Figure 1: Perovskite solar cell design

Figure 2: Leaf-templated perovskite schematic for artificial photosynthesis

Figure 3: Ice templating schematic

Figure 4: X-ray diffraction data

Figure 5: SEM images for “Fast Cool” samples

Figure 6: SEM images for “Slow Cool” samples

Figure 7: Rhodamine-B degradation with time

Figure 8: Band gap determination

Figure 9: Energy-dispersive X-ray spectroscopy data

VOLUME 2

Figure 1: MSNP Synthesis Schematic

Figure 2: Functionalization Schematic

Figure 3: TEM Image of MSNPs

Figure 4: Zeta Potential Measurements

Figure 5: Dynamic Light Scattering (DLS) Measurements

Figure 6: Controlled Release in Un-functionalized MSNPs

Figure 7: Controlled Release in Functionalized MSNPs

LIST OF TABLES

VOLUME 1

Table 1: BET Data

THESIS MOTIF

Nanoparticles have been studied for decades because of their uniquely strong ability to alter properties of composite materials and to catalyze reactions. One characteristic that makes nanoparticles so useful is their inherently high surface area to volume ratio. This thesis presents the development of processes for the syntheses of two distinct nanoparticle systems, and exhibits their implementation into materials that have hierarchical structure, taking their already high surface area to a heightened level. In Chapter 1, the structure provides large macropores that facilitate mass transport, and smaller mesopores for surfaces that can provide able reaction sites. The high surface area to volume ratio of the material presented in this part is promising for photoactivation applications. In Chapter 2, the structure involves surface-functionalized, ultra-small particles that have even smaller mesopores within. Acting as candidates for therapeutic delivery carriers, the particles have high pore volume that allows for efficient payload delivery but are small enough to be transported into body cells for targeted delivery. With high surface area and pore volume compared to bulk, the systems presented in this thesis provide an advanced level of efficiency, executing their function in an improved manner while requiring less material to do so.

CHAPTER 1

HIERARCHICALLY POROUS STRONTIUM TITANATE FOR PHOTOACTIVATION

ABSTRACT

Sub-10 nm strontium titanate (SrTiO_3) particles were synthesized by a novel and facile sol-gel process. These particles were templated with polystyrene nanoparticles (~50 nm) and ice crystals via a freeze-casting technique. Heat treatment simultaneously annealed the SrTiO_3 and removed the polystyrene template. The resulting materials show hierarchical structures consisting of organized 10-100 μm macropores and uniform 50 nm mesopores. In a photodegradation study, these structures induced 100% degradation of rhodamine-B after only one hour of sunlight exposure. This hierarchically porous SrTiO_3 proves to be promising for increasing efficiency in photocatalysis, which can be used for CO_2 reduction and hydrogen fuel generation. Additionally, this material provides a viable substitution for mesoscopic TiO_2 to improve efficiency in perovskite solar cells, which make up an exciting emerging technology.

INTRODUCTION

Perovskite solar cells make up the fastest growing emerging photovoltaic devices to date. They have been shown to have remarkable charge carrier diffusion rates, among other advantages¹. Recently a certified efficiency of 20.1% has been reached with halide perovskite sensitized solar cells. Aside from optoelectronic properties that compete with state of the art photovoltaics, perovskite solar cells offer solution-processed devices for more economical production². The light absorbing layer of these devices consists of an organo-lead halide that is spin-coated on an electron transport layer. This is sandwiched by a hole transport layer and electrodes. Figure 1 is a schematic of the design of a perovskite solar cell³.

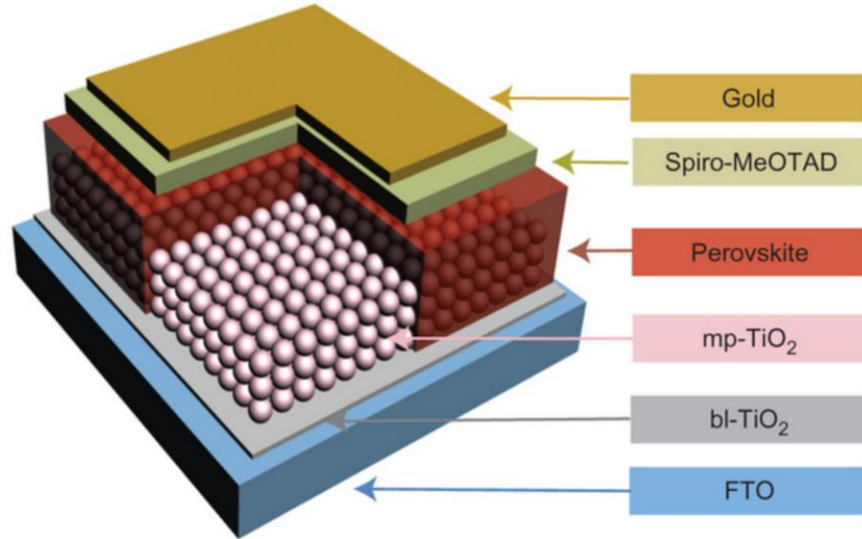


Figure 1. A schematic of the typical perovskite solar cell design (Li *et al.*)³.

Thus far, variations of these perovskite cells have nearly all used mesoscopic TiO₂ as the electron transport layer. However, this TiO₂ provides limited charge transfer efficiency at the interface with the perovskite absorbing layer. This drawback may be attributed to charge recombination at the interface, the difference in crystal structure at the interface, and non-ideal flat band edge potentials. Also, one of the most discussed limitations of these devices is the photochemical instability, which has been attributed to the TiO₂. A recent publication has suggested that these issues can be alleviated by substituting TiO₂ with SrTiO₃⁴.

With versatile electromagnetic properties and robust chemical stability, SrTiO₃ has been used in a wide variety of applications, including microelectronic devices⁵⁻⁸, optical switches⁹, memory, microcapacitors¹⁰, and photocatalysis^{11,12} along with photovoltaic cells^{13,14}. It is a perovskite, and thus more closely matches the crystal structure of the sensitizer used in perovskite cells compared with TiO₂. With room temperature electron mobility in the range of 5-8 cm²V/s compared to 0.1-4 cm²V/s of TiO₂, it is also a better charge carrier. The substitution also reduces destructive charge recombination due to a higher dielectric constant¹⁵. Lastly, the slightly higher flat band edge potentials of SrTiO₃ are more suited for charge transport across the interface with the organo-lead halide sensitizer⁴.

Due to its more versatile crystal structure, SrTiO₃ has been doped to tune and optimize its optoelectronic properties¹⁶. One exciting property that can be achieved is ferroelectricity, which allows for the simultaneous photo-generation and transport of charge carriers in photovoltaic cells¹⁷. This is due to an induced and remnant charge polarization, which also helps prevent charge carrier recombination¹⁸. In this light SrTiO₃ can supplement the current density produced by the halide perovskite sensitizer by absorbing light in the UV range, while also improving upon the efficiency of electron transport to the anode.

SrTiO₃ can also be doped to optimize the material for hydrolysis of water using light as the only energy source¹⁹⁻²¹. Instead of using smaller band gap materials which have limited range of potential for catalyzing reactions, large band gap photocatalysts can be more versatile. By adding dopants, additional donor and acceptor levels can be introduced within the wide gap allowing for absorption of visible light but with a material with more broad potentials in the active region of the bands.²² Along with several other photocatalyst materials, doped SrTiO₃ can catalyze hydrogen evolution in an aqueous solution without the need for input voltage. However, this usually requires sacrificial reagents. In one study, SrTiO₃ was doped with Rh, which narrowed the band gap to produce a prominent absorption band in the visible region. With platinum as a co-catalyst and methanol as the reducing agent, hydrogen production with a 5.2% quantum yield was observed²³. Another group was able to produce stoichiometric amounts of hydrogen and oxygen simultaneously using Rh-doped SrTiO₃ for the evolution of hydrogen and other photocatalyst powders for oxygen production. The combination of catalysts that were chosen, along with the use of an acidic solution, enabled efficient water splitting without the use of sacrificial reagents²⁴. This mechanism theoretically avoids the need to replenish any part of the system, so the hydrogen-generating reactor solution can be left working in sunlight with relatively low maintenance.

Another method for converting solar energy to chemical energy is via CO₂ reduction. Photocatalysts that can achieve this with reasonable efficiency are highly valued because the process can simultaneously produce energy and help remove the most prevalent greenhouse gas from the atmosphere. Some groups have conducted “artificial photosynthesis” with SrTiO₃, using water as a proton source and electron donor. One such study achieved a 0.14% conversion efficiency from solar energy to chemical

energy using a hybrid system with reduced SrTiO₃ as a photoanode²⁵. While photocatalytic performance can be improved using hybrid systems, new doping elements, and sacrificial oxidative and reductive agents, they are ultimately limited by how efficiently the light can be absorbed and how fast the generated charge carriers can be transported. These factors are dependent on the physical structure of the photocatalyst.

A recent pioneering investigation into artificial photosynthesis has shed new light on the importance of the physical structure of the material that is used as a catalyst. This study used an actual leaf as a template for morphing perovskite titanates - including SrTiO₃ - into three-dimensional architectures that mimic the leaf's optimized biological structure²⁶. A schematic from their work depicting the CO₂ reduction process is included in Figure 2.

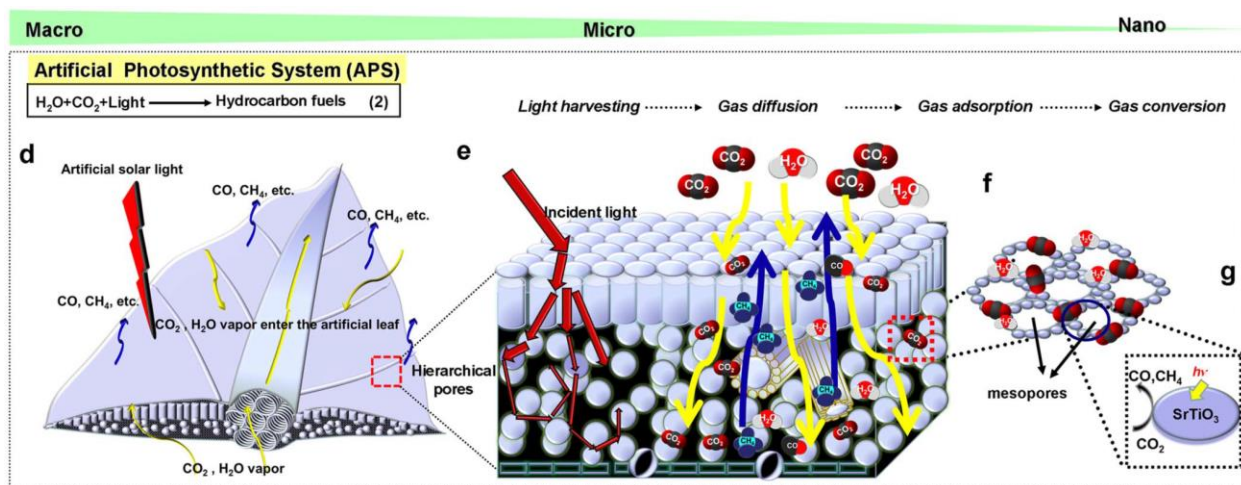


Figure 2. A schematic showing the process for CO₂ reduction in a leaf-templated artificial photosynthesis system (Zhou *et al.*). The architecture allows for mass transport at the macroscale (left) and photo-conversion at the microscale²⁶.

The leaf-architected SrTiO₃ was able to produce methane at a rate approximately four times greater than powdered SrTiO₃ under the same photocatalysis conditions. This work has advanced the design of photocatalyst materials with both macro and micro-scale architecture, a strategy that addresses both the physical and chemical demands of a high-performance solar energy conversion system.

Acknowledging the need for consideration of material geometries at multiple scales, previous members of the Giannelis group at Cornell University have developed an ice-templating technique to

produce hierarchically porous structures in a rapid, simple, and reproducible manner²⁷⁻³⁰. This technique has allowed the production of materials with ultra-high surface areas, which allow for much improved efficiencies for energy storage³¹, photovoltaic cells³², and reaction catalysts³³. The key to their performance is the use of macropore geometries for improved mass transport and meso- and micropores for high surface area to increase capacitance or photoconversion. Fu *et al.* produced activated carbon structures with surface areas in excess of 2000 m²/g with this method³⁴. The ice templating technique uses a dispersion of a precursor and a hard template material that is flash-frozen in liquid N₂ and then freeze dried. The sublimed ice crystals leave behind macropores, while the hard template material provides mesopores (2-50 nm) and in some cases micropores (< 2 nm) after heat treatment or etching. For the work presented in this thesis, the precursor material consists of SrTiO₃ nanoparticles and the template material is polystyrene latex.

Nanoparticles have been used as catalysts for decades owing to their inherently high surface area to volume ratio. The majority of current syntheses for SrTiO₃ nanoparticles make use of a hydrothermal technique, which includes high temperature and tedious processing conditions³⁵. We have developed a facile sol-gel synthesis to produce ultra-small, monodisperse SrTiO₃ particles. By implementing these particles into a hierarchical structure via the ice templating technique, the SrTiO₃ surface area, and thus the photocatalytic activity of the material can be vastly improved. The ice templating mechanism with SrTiO₃ nanoparticles as the precursor material is depicted in Figure 3.

By producing SrTiO₃ in a hierarchical structure that allows for good mass transport via macropores and higher surface area via mesopores, this work provides yet another improvement upon mesoscopic TiO₂ as the electron transport layer in state of the art perovskite solar cells, aside from the improved optoelectronic properties of SrTiO₃ over TiO₂ as presented previously. The currently used mesoscopic TiO₂ is a sintered powder composed of nanoparticles on the order of 100 nm in diameter³⁶. The porosity is limited to the surface area of these compressed spheres. Replacing TiO₂ with a perovskite that has more favorable optoelectronic properties while also increasing the surface area available for charge generation and transport is likely to significantly elevate the performance of perovskite solar cells.

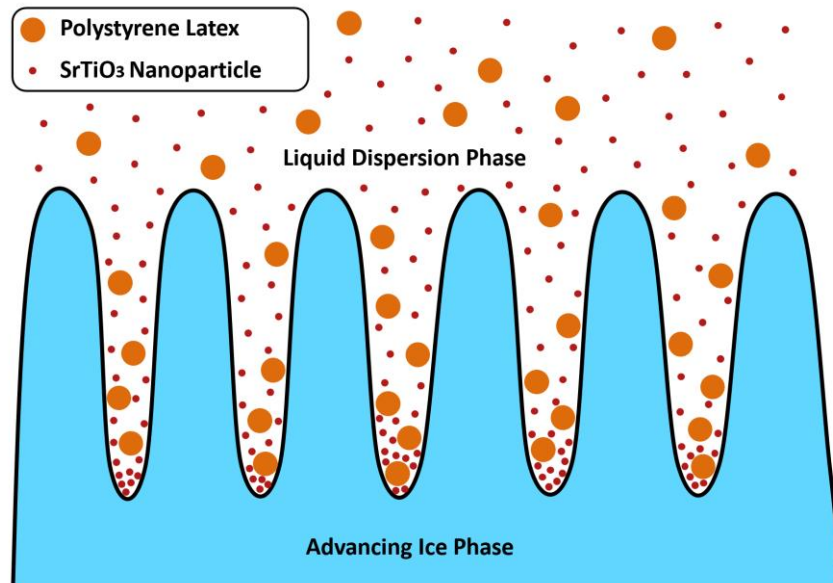


Figure 3. A schematic showing the freeze casting technique developed previously by the Giannelis group with polystyrene latex as the template material and SrTiO₃ nanoparticles as the precursor material.

To simulate the photocatalytic activity of the hierarchically porous SrTiO₃ (HPSTO), a study was conducted to measure the oxidation of rhodamine-B under sunlight exposure. The performance of the HPSTO was compared to that of SrTiO₃ nano-powder purchased from Sigma Aldrich. The purchased SrTiO₃ was significantly outperformed, giving evidence to the utility of the uniquely structured HPSTO material.

EXPERIMENTAL

SrTiO₃ Synthesis. A sol-gel method was developed for the synthesis of monodisperse, sub-10 nm SrTiO₃ particles. A solution of SrCl₂, acetic acid (25 wt%), and water was added dropwise to a stoichiometric amount of titanium(IV)bis(ammonium lactato)dihydroxide 50% solution under magnetic stirring. The resulting solution was heated in a 70 °C oil bath for 24 hours. Dialysis using 3.5k molecular weight plastic membranes was performed for 2 days to remove unreacted precursors. The particle size was measured using dynamic light scattering (DLS).

Polystyrene Latex Synthesis. A radical emulsion polymerization was used to synthesize polystyrene latex nanoparticles. The particles were used as a template material to leave behind mesopores in the HPSTO. 3.6 g of styrene was mixed with 0.8 g of sodium styrene sulfonate, 0.1 g sodium bicarbonate, and 70 g water. This mixture was emulsified with high rpm magnetic stirring in a 70 °C oil bath. The flask was sealed with a rubber stopper to prevent oxygen from entering the system during polymerization. A separate solution of 0.1 g sodium persulfate and 5 g water was injected into the styrene emulsion to initiate radical polymerization. The emulsion was heated for 24 hours and then dialyzed for 2 days. DLS was used to measure the size distribution.

Ice Templating. The polystyrene nanoparticles were mixed with the SrTiO₃ nanoparticles in a range of discrete wt % ratios. The samples of aqueous dispersions were sonicated for 10 minutes to ensure a uniform distribution. Two sets of samples were separated based on freezing rate. The “fast-cool” samples were precooled in a -20 C freezer for 20 minutes, just before they would begin to freeze. The samples were sonicated again for 1 minute. To prepare for freeze drying, a sample was poured into a thin aluminum boat which was submerged in liquid N₂ for 30 seconds. For the “slow cool” samples, the Falcon tubes containing the dispersions were simply submerged in liquid N₂ for thirty seconds. The flash-frozen dispersions were then freeze dried for 2 days to sublime the ice, leaving ~ 10-100 μm macropores where the ice crystals vaporized.

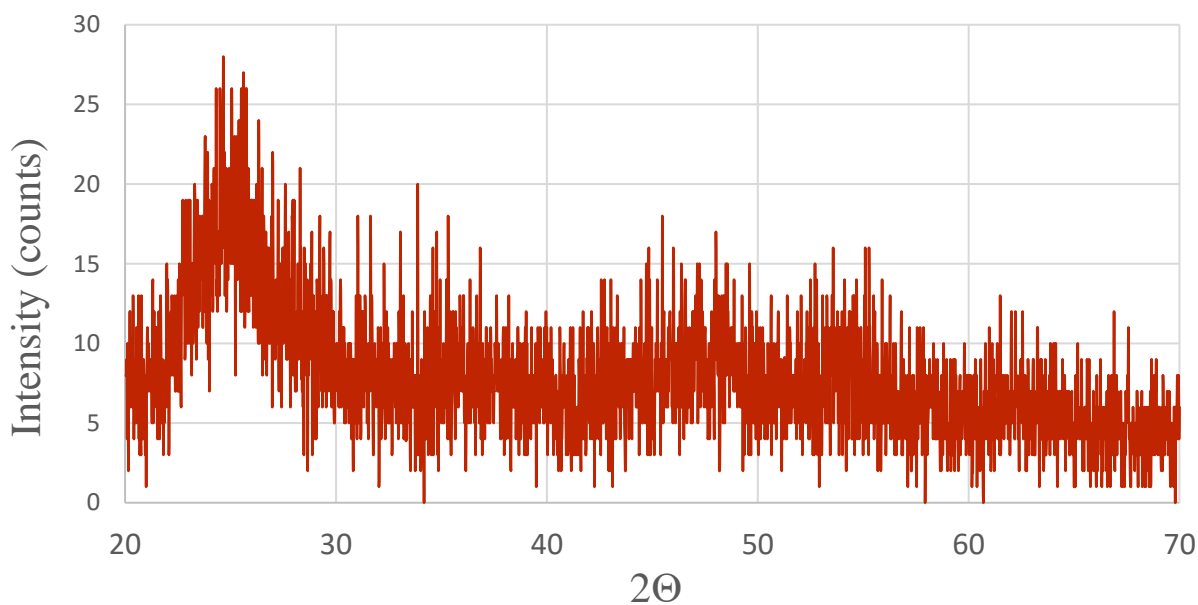
Heat Treatment and Sintering. The samples were subjected to controlled atmosphere heating at 530 °C for 2 hours. The samples were heated under inert N₂ gas so that the polystyrene latex could carbonize, producing a carbon backbone to promote structural stability before the carbon would be burned away. Later the samples were heated in air at 470 °C for 10 hours. This heating step completely burned away the carbon. The combined heat treatment annealed the SrTiO₃ nanoparticles, and XRD was conducted to reveal a highly crystalline perovskite structure.

Photodegradation of Rhodamine-B. To simulate the photocatalytic activity of HPSTO, a photodegradation study was conducted using rhodamine-B dye. 0.2 g/L HPSTO was dispersed in a 1 μM

solution of rhodamine-B. A similar dispersion using commercial SrTiO₃ nano-powder purchased from Sigma Aldrich was also prepared. The Aldrich SrTiO₃ powder was composed of ~100 nm particles. These two dispersions were shaken and sonicated in the dark for 30 minutes each to equilibrate. They were then placed in transparent quartz vials and exposed to midday sunlight along with a control vial that contained the dye without catalyst. Aliquots of each vial were removed at time intervals between 30 minutes and 6 hours. The absorbance spectra of the aliquots were measured immediately and the relative concentration of rhodamine-B was calculated from the maximum of the absorption peaks.

RESULTS

Nanoparticle Characterization. DLS data showed that the SrTiO₃ synthesis could produce sub 10 nm particles. The SrTiO₃ used for the HPSTO samples were 3.5 nm and had a polydispersity index of 0.25. The polystyrene latex synthesis was optimized to consistently produce ~ 50 nm particles. The polystyrene used for the HPSTO samples were 55 nm and also had a polydispersity index of 0.25 (measured by DLS). XRD was performed on the SrTiO₃ particles before heat treatment, and was also performed on the HPSTO. The diffraction plots for both are given in Figure 4. The HPSTO shows high perovskite crystallinity, while the un-annealed nanoparticles are amorphous.



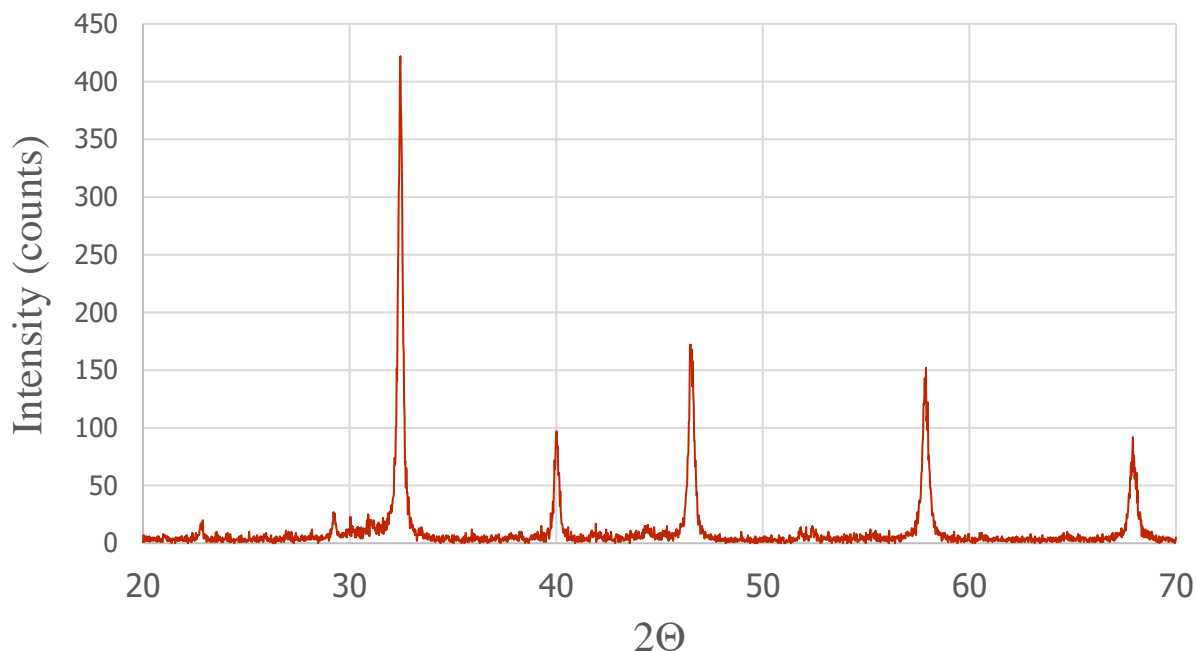
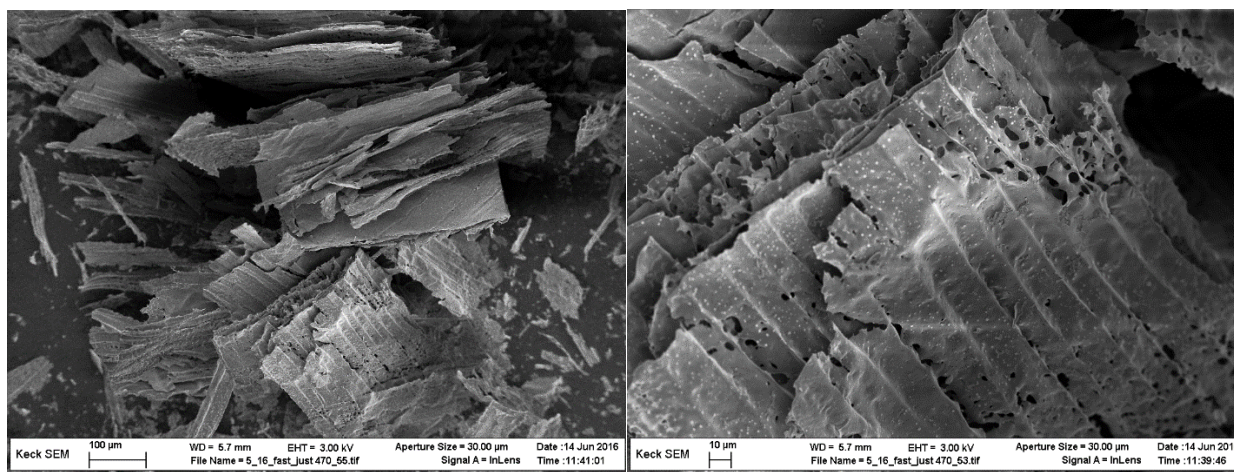


Figure 4. XRD data showing amorphous structure in the as-synthesized SrTiO₃ nanoparticles (top) and diffraction peaks characteristic of perovskite structure in the HPSTO (bottom).

Pore Structure Characterization. The HPSTO samples were imaged under scanning electron microscopy (SEM). For the “fast-cool” samples, linear and fairly uniform 10-20 μm macropores were present in the HPSTO. In some cases these macropores were uniform in two directions, resulting in nanosheets. Along with all other macrostructure, these nanosheets contained uniformly distributed 50 nm mesopores. Figure 5 includes a sampling of the “fast-cool” HPSTO SEM images.



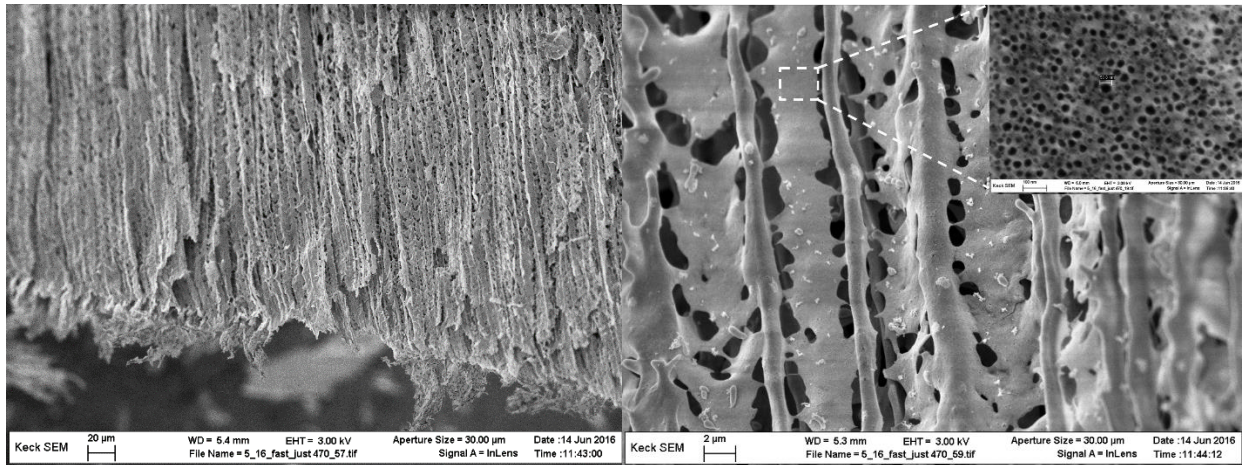


Figure 5. SEM images of HPSTO, showing nanosheets (top) and bulk macroporous structure (bottom). Mesopores of 50 nm diameter are shown (inset).

The uniform and continuous mesopores are important because these contribute most to the ultimate surface area of the material. While the macropores contribute less to the total surface area, they do provide for mass transport. This architecture promotes efficiency as uncatalyzed species can easily diffuse through the HPSTO to replace those which have already been catalyzed.

The edges of the macropores form ridges of continuous SrTiO_3 . In some cases these ridges have reduced mesoporosity. It is possible that the advancing ice crystals squeezed out the polystyrene latex template, leaving only SrTiO_3 at these junctions. This phenomenon could potentially be favorable, however. With HPSTO replacing TiO_2 as the electron transport layer in perovskite solar cells, it is important to have good connections across the material. The macropore edge structure seems to be favorable for charge carrier transport.

For the “slow-cool” HPSTO samples, the SEM images show large, non-uniform macropores of approximately 100 µm in diameter. These images are shown in Figure 6. Based on the SEM images for both sets of samples, it is clear that a slower freezing rate results in larger macropores due to larger ice grains during freeze casting. This is an important parameter for promoting mass transport in the HPSTO material.

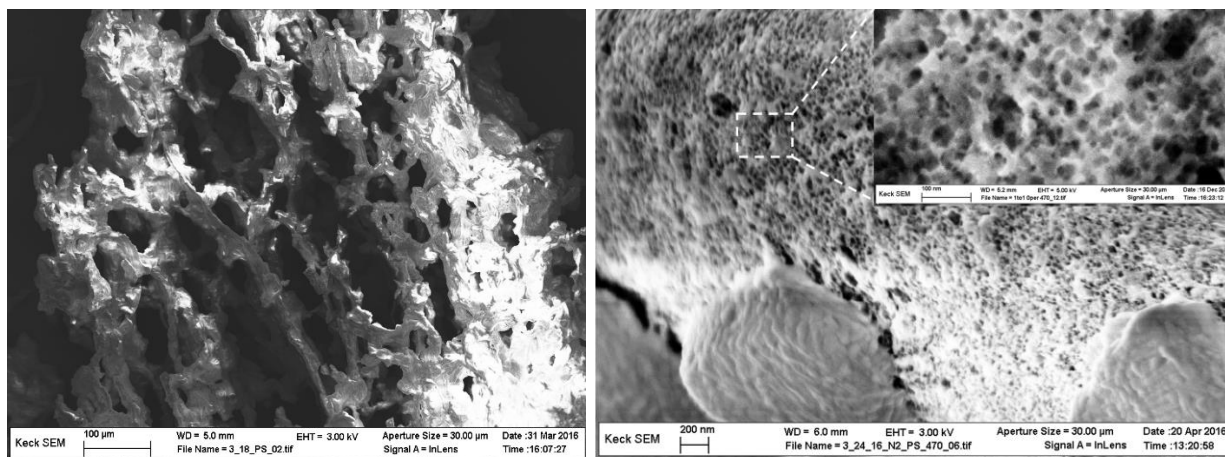


Figure 6. SEM images of the “slow cool” HPSTO samples, with macropore (left) and mesopore (right) structure shown.

The pore structure was further characterized using BET. An ASAP 2460 BET was used to conduct N_2 adsorption measurements, providing surface area, mesopore volume, and average pore size. These measurements were conducted for various wt % ratios of $SrTiO_3$:polystyrene, and the results are included in Table 1. A trade-off exists between the precursor and template ratios: Increasing the relative amount of polystyrene particles provides more template for mesopores, but less $SrTiO_3$ decreases the physical stability of the HPSTO, because the PS template does not contribute to the structural integrity of the material. Previous studies have shown that the optimal surface area for these ice templated materials exists when the mesopores make up 50% of the bulk volume. This equates to a 5:1 $SrTiO_3$:polystyrene ratio. It is clear from the BET data that the optimal ratio exists between 2:1 and 3:1 $SrTiO_3$:polystyrene. It is likely that many of the polystyrene particles that were burned off did not contribute to the mesoporosity, and thus a higher amount was needed relative to $SrTiO_3$ to yield increased surface area.

While the surface area values listed in Table 1 are still marginally better than the surface area of the meso- TiO_2 used in perovskite solar cells, another batch of samples yielded surface areas in excess of $300 \text{ m}^2/\text{g}$. Considering that the bulk density of $SrTiO_3$ is $4.81 \text{ g}/\text{cm}^3$, this is an exciting result. Future work will focus on optimizing conditions to maximize the surface area.

Wt% Ratio SrTiO ₃ :PS	BET Surface Area (m ² /g)	Mesopore Volume (cm ³ /g)
0.5:1	17	0.12
1:1	36	0.35
2:1	62	0.44
3:1	57	0.44
5:1	42	0.38
8:1	52	0.27

Table 1. BET surface area and mesopore volume measured for HPSTO samples of varying SrTiO₃:polystyrene ratios.

Photodegradation Results. The absorption spectrum of the HPSTO was measured in order to determine the band gap and to visualize the light absorption capacity of the material. The absorption spectrum is included in Figure 7.

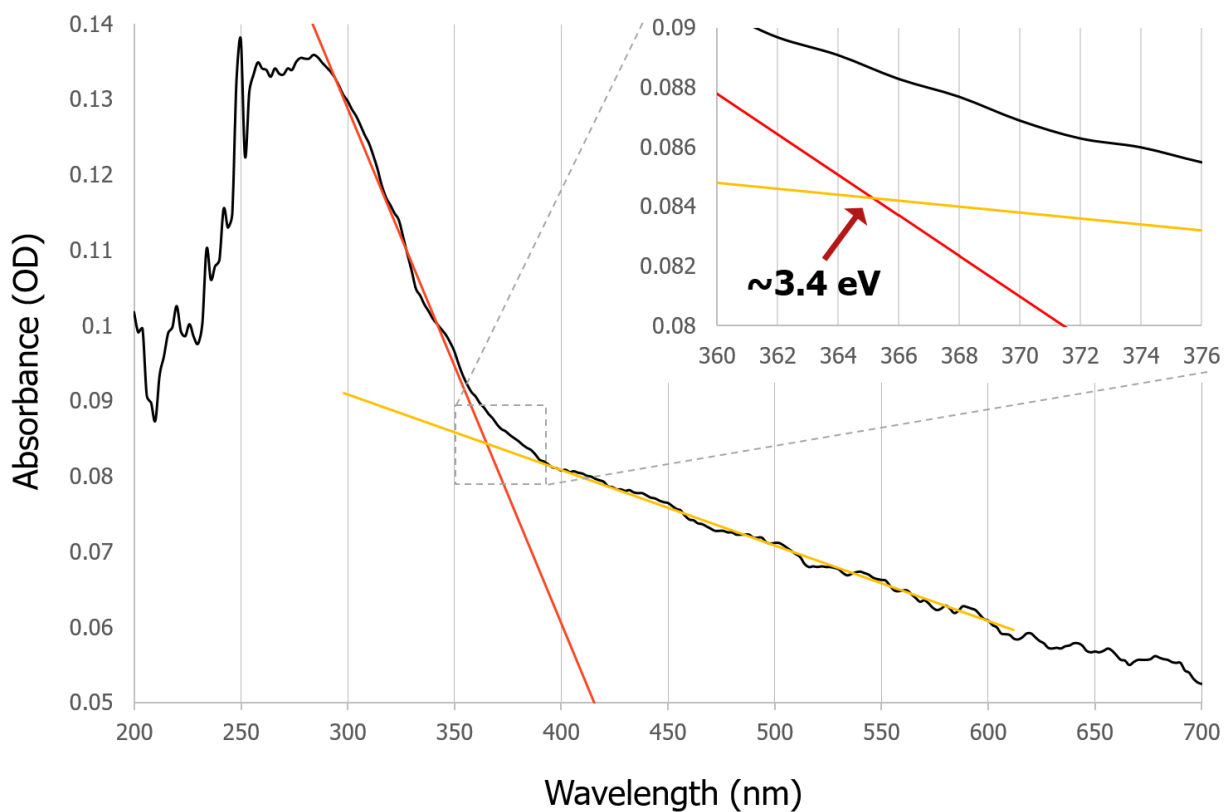


Figure 7. The absorption spectrum of a sample of HPSTO. Linear approximations are included for the two different slopes, and the inset provides a narrower glance at their intersection.

The band gap was determined by taking the intersection of linear approximations of the two portions of the spectrum. This point occurred near 365 nm, which is equated to approximately 3.4 eV. This determination is slightly larger than the pure, bulk band gap of SrTiO₃ which is 3.2 eV. Potential reasons for why this is true for the HPSTO samples are discussed ahead.

The HPSTO significantly outperformed the Sigma Aldrich nano-powder at catalyzing the oxidation of rhodamine-B. Figure 8 is a plot of the concentration of rhodamine-B with time as the dye oxidized in sunlight over the course of 6 hours. The HPSTO catalyzed the 100% degradation of rhodamine-B within only 1 hour. To date, similar studies report 100% degradation only after 6 hours. Because the HPSTO catalyzed at a rate such significantly faster than the nano-powder form, it is likely that the unique, hierarchical porous structure is what makes the HSPTO such an efficient catalyst. However, other factors contributing to the high photocatalytic efficiency must also be considered.

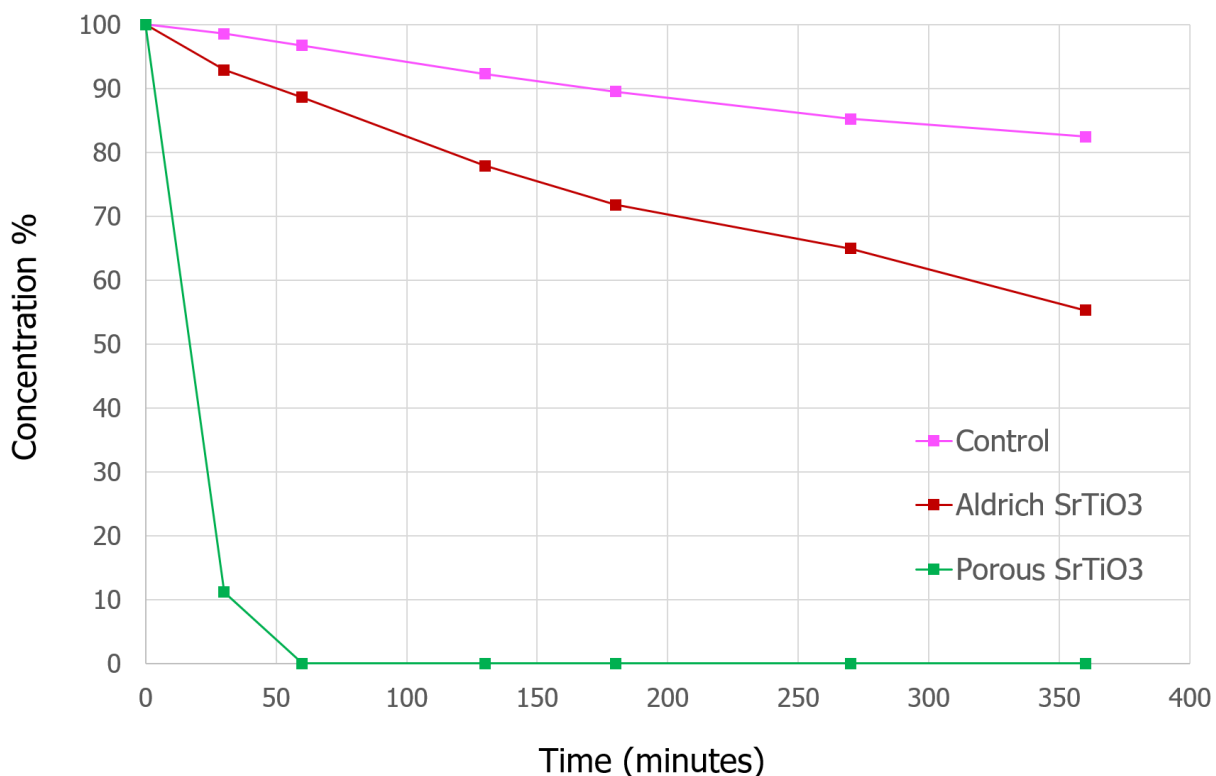


Figure 8. Concentration of rhodamine-B as a function of time exposed to sunlight for just dye (control), Aldrich SrTiO₃, and porous SrTiO₃ (HPSTO). Concentration was measured by comparing the relative size of rhodamine-B absorbance peaks at each time interval.

One such consideration is the potential for impurities/dopants to impact the electronic properties of the SrTiO₃. One such impurity is chlorine, which is an anion introduced in the synthesis recipe used to produce the SrTiO₃ nanoparticles. Oxygen binds to the cations of titanium and strontium much more favorably than chlorine, and during the synthesis of the SrTiO₃ the oxygen atoms are already bound to the titanium. Additionally, the synthesis is carried out in open atmosphere, so oxygen is readily available and chlorine is not likely to replace it in the SrTiO₃ lattice. However, the chlorine remains in solution after the SrCl₂ dissolves, and not all the chlorine can be removed during the dialysis (at least in the short time attempted here) that is completed after the synthesis process. The chlorine ions remain in solution until the freeze casting procedure, and after the water is removed it is likely that adsorbed chlorine salts remain on the HPSTO surface. The first heat treatment step is performed under a nitrogen atmosphere, which removes the otherwise readily available oxygen within the air. In this oxygen-lean environment chlorine substitutions in oxygen positions are possible, and 530 °C provides enough energy for adsorbed chlorine to enter the crystal structure while the SrTiO₃ nanoparticles are annealing. Another possibility is that the chlorine is simply physisorbed on the high surface area perovskite. EDX analysis of the HPSTO is shown in Figure 9, and this characterization revealed the high presence of chlorine within the material.

As an impurity, chlorine would replace oxygen in the SrTiO₃ lattice and induce p-type doping. A previous study investigated the effect of chlorine doping on the photocatalytic activity of TiO₂³⁷. SrTiO₃ and TiO₂ have similar band gap structures, so it is reasonable to compare their responses to dopants. Results from the study showed that the band gap decreased with the addition of chlorine dopants after calcination at 300 °C. This decrease in band gap allowed for absorption in the visible range and increased the efficiency of photocatalytic degradation of phenol. It is possible that chlorine substitutions in the HPSTO contributed to the ability for the material to absorb visible light, which was why it performed so well in the photocatalytic degradation of rhodamine-B.

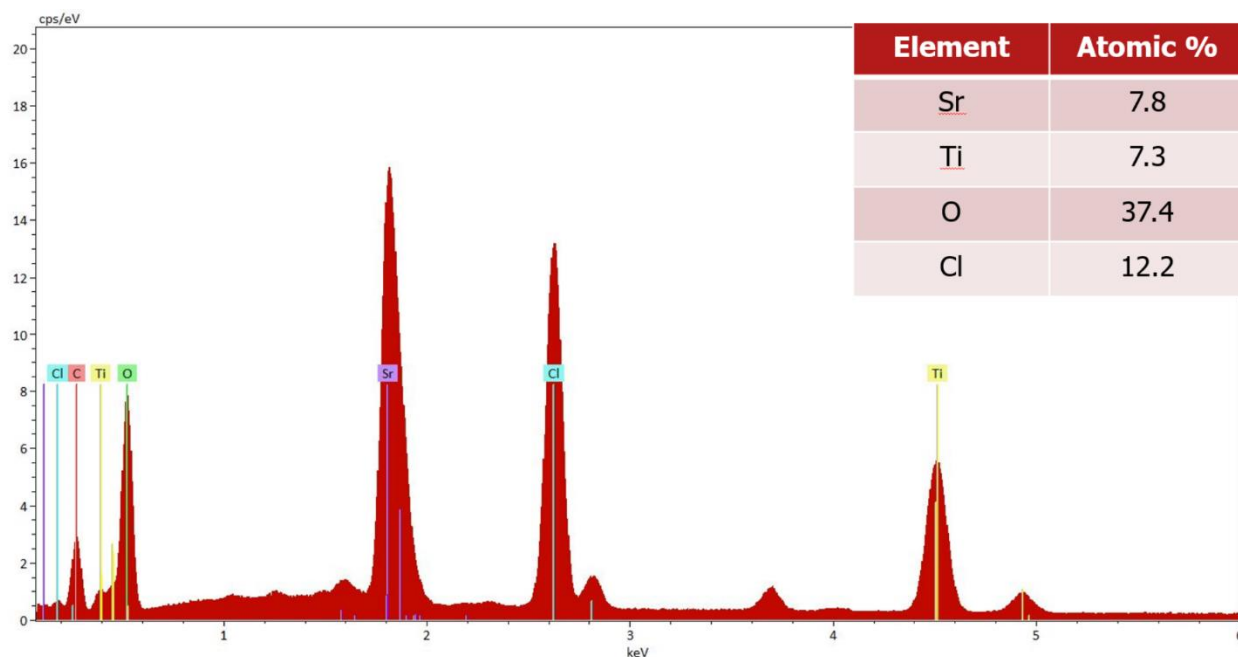


Figure 9. Energy-dispersive X-ray spectroscopy analysis of an HPSTO sample. The table inset on the top right shows the presence of relevant elements in atomic percent.

Yet another potential impurity that could have given rise to the high photocatalytic efficiency seen in this rhodamine-B degradation study is carbon. The process by which carbon could have been introduced into the SrTiO_3 lattice is slightly more obvious, and theoretically more likely, than that of chlorine. The polystyrene nanoparticles provides a precursor to carbon black, which will have been produced during the heat treatment under a controlled nitrogen atmosphere. Without oxygen, instead of simply burning away, the polystyrene carbonizes, and this is a potential source for carbon substitutions within the SrTiO_3 lattice, especially under high heat conditions. A study used density functional theory calculations to predict the likelihood of carbon substitutions for each of the elements in the SrTiO_3 lattice, and provided an analysis of the resulting electronic properties³⁸. The researchers found that it is more favorable for the carbon to replace titanium in the lattice, a substitution which only provides a limited effect on the electronic properties of the material. However, they found that there is also a significant likelihood for the carbon to replace strontium cations. Additionally, especially under oxygen-lean conditions, there is a chance for the carbon to substitute into oxygen positions. The carbon substitutions in oxygen and strontium positions are

“electronically active”, meaning they have a significant impact on the electronic properties of SrTiO₃. For example, for each carbon that replaces oxygen, two electrons are removed from the highest occupied molecular orbital, resulting in more of a partially unfilled band and inducing conductivity. This would allow for increased transport of charge carriers, which could increase the efficiency of rhodamine-B oxidation. Another finding reported in their study is that, while they did not actively alter the electronic properties, carbon substitutions on titanium sites slightly increased the band gap. This can explain the elevated band gap of the HPSTO samples reported in Figure 8. It is clear that impurities play a large role in the optoelectronic properties of SrTiO₃, and thus are important for first understanding and subsequently optimizing the efficiency of SrTiO₃ photocatalyst materials.

One direct application of the HPSTO photocatalyst, which has been evidenced directly by this study, is for the removal of dyes from contaminated water. There are approximately 700,000 tons of industrial dyes produced each year, and as much as 20% of that amount can contaminate the water, which has a high impact on the environment and drinking supply. Environmental standards of governing bodies regulate the amount of contamination that results from textile companies, so these companies have sought solutions for methods of removing the dyes³⁹. Thus, there is a financial as well as environmental motivation for the use of photocatalysts to degrade dyes, and the degradation rate catalyzed by the HPSTO in this study makes this material highly valuable for the textile industry. The high photocatalytic efficiency shown in this thesis work can be projected to even further applications, and one that is exciting as well as promising is the use of HPSTO as a replacement for mesoscopic TiO₂ in perovskite solar cells.

REFERENCES

1. Stranks, S. D.; Eperon, G. E.; Grancini, G.; Menelaou, C.; Alcocer, M. J. P.; Leijtens, T.; Herz, L. M.; Petrozza, A.; et al. *Science* **342** (6156): 341–344. October 2013.
2. Eperon, Giles E.; Burlakov, Victor M.; Docampo, Pablo; Goriely, Alain; Snaith, Henry J. *Advanced Functional Materials* **24** (1): 151–157. 2014.
3. Xiong, L. M. et al. *Nature Chemistry* **7**. 703-711. 2015.
4. Bera, A.; Wu, K.; Sheikh, A.; Alarousu, E.; Mohammed, O.; Wu, T. *J. Phys. Chem. C*. 118 (49): 28494-28501. 2014.
5. R. V. Shende, D. S. Krueger, G. A. Rossetti, and S. J. Lombardo. *J. Am. Ceram. Soc.*, 84, 1648–50 (2001).
6. F. M. Pontes, E. R. Leite, E. J. H. Lee, E. Longo, and J. A. Varela. *J. Eur. Ceram. Soc.*, 21, 419–26 (2001).
7. J. Cukauskas, S. W. Kirchoefer, W. J. DeSisto, and J. M. Pond. *Appl. Phys. Lett.*, **74**, 4034–6(1999).
8. Shanthi and D. D. Sarma. *Phys. Rev. B*, **57**, 2153–8 (1998).
9. Z. Yang, H. B. Lü, F. Chen, T. Zhao, and Z. H. Chen. *J. Cryst. Growth*, **227–228**, 929–35 (2001).
10. Tabata and T. Kawai. *Appl. Phys. Lett.*, **70**, 321–3 (1997).
11. Y. Li, X. P. Gao, G. R. Li, G. L. Pan, T. Y. Yan, and H. Y. Zhu. *J. Phys. Chem. C*, 113, 4386–94 (2009).
12. M. Miyauchi, A. Nakajima, A. Fujishima, A. Hashimoto, and T. Watanabe. *Chem. Mater.*, 12, 3–5 (2000).
13. Call, R. W. et al. *ACS Appl. Mater. Interfaces*, **2016**, 8 (19), pp 12282–12290.
14. Huang, W. et al. *J. Am. Ceramic Soc.* 99 (1). 226-233. 2015.
15. F. M. Pontes, E. J. H. Lee, E. R. Leite, E. Longo, and J. A. Varela. *J. Mater. Sci.*, 35, 4783–7 (2000).
16. Wang, J. S. et al. *Solid State Sciences*. 11 (1). 182-188. 2009.
17. Dawber, M.; Rabe, K. M.; Scott, J. F. *Physics of Thin-Film Ferroelectric Oxides*. *Rev. Mod. Phys.* 2005, **77**, 1083–1130.
18. Haeni, J. et al. *Nature*. 430. 758-761. 2004.
19. Wrighton, M. S.; Ellis, A. B.; Wolczanski, P. T.; Morse, D. L.; Abrahamson, H. B.; Ginley, D. S. *J. Am. Chem. Soc.* 1976, **98**, 2774–2779

20. T. Puangpetch, T. Sreethawong, S. Yoshikawac, and S. Chavadej, *J. Mol. Catal. A: Chem.*, 312, 97–106 (2009).
21. Ouyang, S.; Tong, H.; Umezawa, N.; Cao, J.; Li, P.; Bi, Y.; Zhang, Y.; Ye, J. *J. Am. Chem. Soc.* 2012, 134, 1974–1977.
22. Kato, H.; Kudo, A. *J. Phys. Chem. B.* 106 (19). 5029-5034. 2002.
23. Kudo, A. *Int. J. Hydrogen Energy.* 31 (2). 197-202. 2006.
24. Sasaki, Y. *et al. J. Phys. Chem. C.* 113 (40). 17536-17542. 2009.
25. Arai, T.; Sato, S.; Kajino, T.; Morikawa. *Energy Environ. Sci.* 6. 1274–1282. 2013.
26. Zhou, H.; Guo, J.; Li, P.; Fan, T.; Zhang, D.; Ye, J. *Nature.* 3 (1667). 2013.
27. Estevez, L.; Kellarakis, A.; Gong, Q.; Da'as, E.; Giannelis, E. *J. Am. Chem. Soc.* 133 (16). 6122-6125. 2011.
28. Estevez, L.; Dua, R.; Bhandari, N.; Ramanujapuram, A.; Wang, P.; Giannelis, E. *Energy Environ. Sci.* 6. 1785-1790. 2013.
29. Wan, A.; Inal, S.; Williams, T.; Wang, K.; Leleux, P.; Estevez, L.; Giannelis, E.; Fischbach, C.; Malliaras, G.; Gourdon, D. *J. Mater. Chem. B.* 3. 5040-5048. 2015.
30. Williams, T. "Freeze-Casting For Facile Synthesis Of Novel Porous Materials." 2016.
31. Sahore, R.; Estevez, L.; Ramanujapuram, A.; DiSalvo, F.; Giannelis, E. *J. Power Sources.* 297. 188-194. 2015.
32. Tian, Y. *et al. Electrochemistry Comm.* 11 (8). 1603-1605. 2009.
33. Fu, W. *et al. Colloids and Surfaces A.* 289 (1-3). 47-52. 2006.
34. Fu, L.; Qi, G.; Sahore, R.; Sougrat, R.; DiSalvo, F.; Giannelis, E. *Phys. Chem. Chem. Phys.* 15. 19134-19137. 2013.
35. Wei, X. *et al. Journal of the American Ceramic Society.* 91 (11). 3795-3799. 2008.
36. Bi, D. *et al. The journal of physical chemistry letters.* 4 (9). 1532-1536. 2013
37. Chen, H.; Long, M.; Xu, J.; Cai, W. *Chinese J. of Catalysis.* 27 (10). 890-894. 2006.
38. Al-Hadidi, M. *et al. Modeling and Sim. In Mat. Sci. Eng.* 23 (1). 2015.
39. Karimi, L. Zohoori, S. *Nanostruct Chem.* 3 (32). 2013.

CHAPTER 2

ULTRA-SMALL MESOPOROUS SILICA PARTICLES WITH pH-SENSITIVE CONTROLLED RELEASE

ABSTRACT

Current small-scale drug delivery systems with controlled release mechanisms are composed of particles or capsules typically > 100 nm, which limits cellular uptake and prevents normal bodily excretion. Here we adapt a synthesis procedure to achieve 15 nm mesoporous silica nanoparticles (MSNPs) with a simple method for adding functionality. The “one-pot” synthesis simultaneously functionalizes and controls the size of the MSNPs by terminating growth with an amino silane compound. DLS and zeta potential measurements show a pH response, confirming that amino silane is successfully grafted to the MSNPs. The MSNPs were loaded with rhodamine-B and the release rate was measured at pH 4.5, 6.0, and 7.4. The functionalized MSNP samples show tunable permeability, with limited release at bodily pH (7.4) and more significant release at lysosomal pH (4.5). These drug delivery systems can be transported within targeted cells and will selectively release the active drug component only upon entering the cell via endocytosis, providing a promising platform for efficient cancer therapy.

INTRODUCTION

Recently there has been interest in the design of drug delivery systems (DDS) with controlled release mechanisms¹⁻⁴. Many of these delivery systems are designed for intravenous injection, which promotes high biodistribution^{5,6} and relatively constant pH (~ 7.4)⁷. Intravenous injection of a DDS also allows for renal excretion, preventing drug carriers from accumulating in certain areas of the body. However, in order to undergo renal clearance the DDS must be sufficiently small – less than 20 nm in diameter⁸.

Silica has been investigated for use in therapeutic applications due to its minimal toxicity⁹ and versatile chemistry¹⁰. In one study, silica nanoparticles were developed with a core-shell architecture that is useful for drug delivery¹¹. Work similar to this is important for the development of “lab on a particle” architectures. These conceptual systems utilize a therapeutic nano-carrier that can integrate multiple functions, including diagnostic tools, target selectivity, and controlled release of the therapeutic payload^{12,13}. Mesoporous silica nanoparticles (MSNPs) have garnered attention as a DDS for their high loading capacity and good biocompatibility, among other advantages¹⁴⁻¹⁸. Ma *et al.* have recently developed a well-controlled method for synthesis of sub-20 nm MSNPs with sustained colloidal and structural stability. This new growth procedure provides an advancement in the state of the art of MSNP synthesis¹⁹.

The goal of the work outlined in this manuscript is to adapt the MSNP synthesis procedure developed by Ma *et al.* to establish a DDS with controlled release functionality. This procedure is presented in Figure 1. In this synthesis method, the growth of the MSNPs is quenched or “capped” by adding PEG-silane. The size of the resulting MSNPs is controlled by the time at which the PEG-silane is added. The PEG end group is used for colloidal stability via steric hindrance.

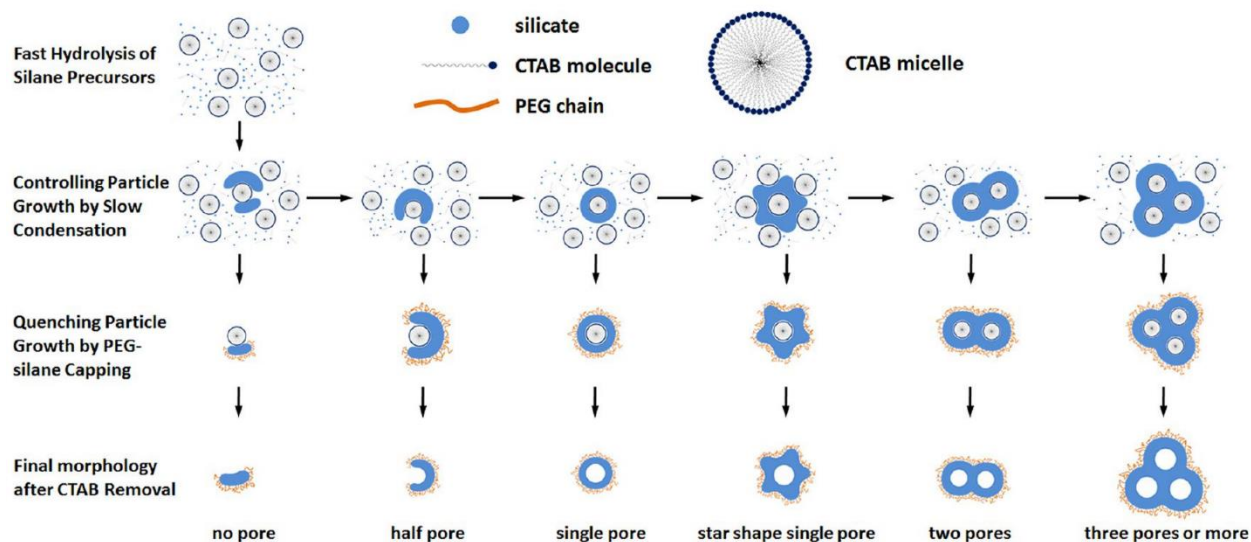


Figure 1: Schematic of the MSNP synthesis mechanism¹⁹.

In this thesis we have adapted the synthesis procedure by Ma *et al.* to develop MSNP particles suitable for the implementation of a novel controlled release system. This adaptation involves the use of (3-Trimethoxysilylpropyl)diethylenetriamine to cap the growth of the particles instead of PEG-silane. A schematic of the functionalization is included in Figure 2. Using amine groups on the ligand allows for the permeability of the MSNPs to be sensitive to pH. At low pH the amine groups become charged and repel each other, increasing the permeability of the MSNP only at pH values below the isoelectric point (~ pH 6). Thus, MSNPs functionalized with (3-Trimethoxysilylpropyl)diethylenetriamine (MSNPs-amine) will be able to release drug contents according to the pH of the environment. The pH response of these particles will be compared to the standard PEG-terminated silane MSNPs via a payload release study.

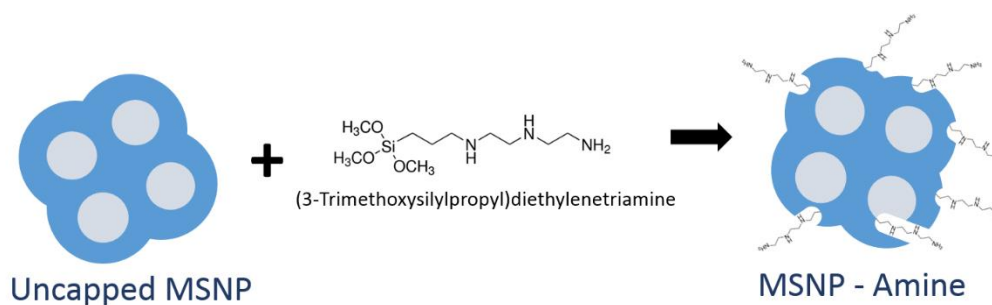


Figure 2: Schematic showing growth capped with (3-Trimethoxysilylpropyl)diethylenetriamine.

Controlling the release of drugs is essential to drug delivery systems. With control over the amount of drug released and the location and duration of the release, more efficient drug delivery can be achieved with minimized side-effects. Additionally, cellular drug delivery can be achieved with small enough particles. When particles are taken up by cells via endocytosis, the particles are transported to lysosomes, which have pH 4.5⁸. The pH-responsive drug carriers can then release therapeutics directly into the cell with minimal release outside the cell, where it may cause undesired effects or at the very least will be excreted and wasted.

EXPERIMENTAL

Mesoporous Silica Nanoparticle (MSNP) Synthesis. The first series of synthesis trials was based on the synthesis method developed by Ma *et. al.* and introduced previously. All chemicals used in synthesis were purchased from Sigma-Aldrich®. 0.23 mmol (84 mg) cetyl trimethylammonium bromide (CTAB) and 0.62 mmol (90.6 mg) L-lysine were added to a 20 mL disposable glass vial and dissolved with 10 mL of deionized water. The CTAB surfactant formed micelles, which became the sites for condensation of silica, which was catalyzed by the lysine. Dissolution was facilitated by placing the vial in a sonication bath for five minutes. Once a clear solution is obtained, a stir bar was added to the vial and the vial was added to an oil bath set at 30 °C and 300 rpm. After waiting five minutes for the temperatures in the system to equilibrate, a micropipette was used to add 0.43 mmol of tetramethylorthosilicate (TMOS) to the vial. The TMOS was added in a slow, drop-wise fashion under continuous stirring in the oil bath to ensure that the ensuing reaction would occur evenly throughout the solution. Hydrolysis and condensation of TMOS produces silica. After 1 hour, 0.11 g polyethylene glycol-silane (PEG-silane) was added to the solution in a similar fashion as the TMOS in order to cap the condensation and limit the size of the MSNPs. The solution was stirred at 30 °C and 300 rpm for 24 hours, at which point the temperature was increased to 80 °C for an additional 24 hours. The sample was then dialyzed to remove unreacted compounds. Particle size measurements were conducted using dynamic light scattering (DLS). It was found that substituting ammonium hydroxide for L-lysine produced more uniform size distributions, and subsequent synthesis preparations implemented this substitution.

A similar procedure as above was used to produce MSNPs functionalized with a pH-sensitive ligand (MSNP-amine). The only difference was that PEG-silane was substituted with (3-Trimethoxysilylpropyl)diethylenetriamine, of which the same molar amount was added. Dynamic light scattering (DLS) was used to measure the size and polydispersity of both MSNP types.

Controlled Release Simulation Study. In preparation for studying the controlled release of the MSNP drug delivery system, the MSNP samples capped with PEG-silane were loaded with a dye molecule

as a surrogate for a potential drug. Rhodamine-B was chosen for controlled release studies because it is moderately hydrophilic, has strong absorbance for good visual approximation of concentration, and is highly soluble in ethanol. To load the dye into the MSNP pores, a stock solution of 2.5 mg rhodamine-B in 10 g ethanol was produced and sonicated for 10 minutes to facilitate complete dissolution. 0.64 g of this solution was added to 7.5 mg of MSNP powder in a 4 mL vial and sonicated for 20 minutes. After adding a stir bar, the vials were placed on a hot plate on low heat (~ 40 °C) and 200 rpm. The vials were left uncapped so that the ethanol solvent would be allowed to evaporate in a fume hood, leaving the rhodamine-B trapped within the pores of the MSNPs.

The release of the MSNP drug delivery system was studied by measuring the release of the rhodamine-B from the MSNPs over time at two different pH levels. To re-disperse the dye-loaded MSNPs, 32 g of deionized water was added and the MSNPs were sonicated for five minutes. This dispersion was separated in half and one aliquot was adjusted to pH 7.4 and the other to pH 4.5 using pH buffers. Similarly, the pH of two beakers filled with 1 L of deionized water was adjusted, and the dispersions were added into dialysis tubing, which was then sealed off and placed into the beakers with corresponding pH values. A stir bar was added to the beakers, and the beakers were covered in aluminum foil to prevent photolysis of the rhodamine-B. The beakers were then placed on stirring plates at 100 rpm. The stirring agitated the dispersion, causing any rhodamine-B that released from the pores of the MSNPs to diffuse across the dialysis membrane and into the water surrounding the tubing. The MSNPs themselves were too large to pass through the membrane, so the concentration of rhodamine-B outside of the dialysis tubing could be taken as the concentration of rhodamine-B released from the MSNPs. 4 mL aliquots were removed from the water surrounding the dialysis tubing at various times over one week to measure the fraction of released rhodamine-B using fluorescence spectroscopy. The aliquots were taken at 4 hours, 8 hours, 12 hours, 16 hours, 24 hours, 44 hours, 68 hours, and 168 hours (1 week). A UV-vis spectrometer was used at excitation wavelength 520 nm to measure the intensity of fluorescence emission across wavelengths from 520 nm to 700 nm for each aliquot. After 1 week the maximum intensity converged, signifying complete release. The fraction of released rhodamine-B for each aliquot was calculated as the maximum intensity of that aliquot

divided by the maximum intensity of the ‘1 week’ aliquot. This experiment was duplicated for the MSNP-amine samples, except for this survey three pH values were compared: 4.5, 6.0, and 7.4

RESULTS

Optimal Ligand Amount. The recipe for the MSNP-amine samples was optimized by varying the amount of (3-Trimethoxysilylpropyl)diethylenetriamine used as the capping molecule, starting with the same molar amount as PEG-silane. MSNP-amine samples had similar size and polydispersity when 126 μL of (3-Trimethoxysilylpropyl)diethylenetriamine was added. This was validated by dynamic light scattering measurements, which were performed for each synthesis iteration.

MSNP Characterization. The size and pore structure of the MSNPs were visualized using transmission electron microscopy (TEM). A TEM micrograph of a MSNP-amine sample is included in Figure 3.

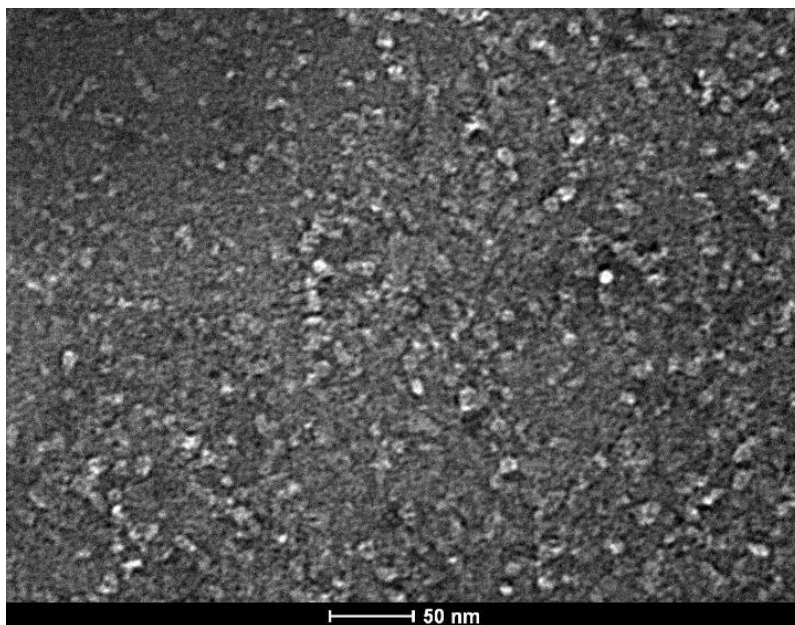


Figure 3: TEM image showing MSNP-amine particles of 10-15 nm

Based on visual observation with TEM, the MSNP size was yet again confirmed to be ~ 15 nm. In the TEM image, the particles vary in their shading and are not uniformly spherical. However, whether or not this reveals the presence of mesopores is inconclusive, and future work including N_2 adsorption measurements will determine whether the mesopores exist. The MSNPs are indeed small enough to enter cells by endocytosis and also be excreted by the body by renal clearance through the kidneys, and the mesopores would allow for loading and unloading of therapeutic payloads.

pH Response Verification. The pH response of the MSNP-amine samples was studied using zeta potential measurements and dynamic light scattering. The zeta potentials of four different preparations of the same MSNP-amine sample are shown in Figure 4. The pH of each preparation ranged from 4.7 to 7.4. At pH 7.4, the MSNP-amine particles have a slightly negative charge, which is consistent with the charge of un-functionalized silica nanoparticles. The charge on the particles begins to increase as the pH decreases, with an isoelectric point at pH 6, and reaching almost 50 mV at pH 4.7. The charge on the particles becomes positive due to the protonation of the amine groups on the ligands. Zeta potential values of 50 mV allow for high enough charge where the charge interactions become significant.

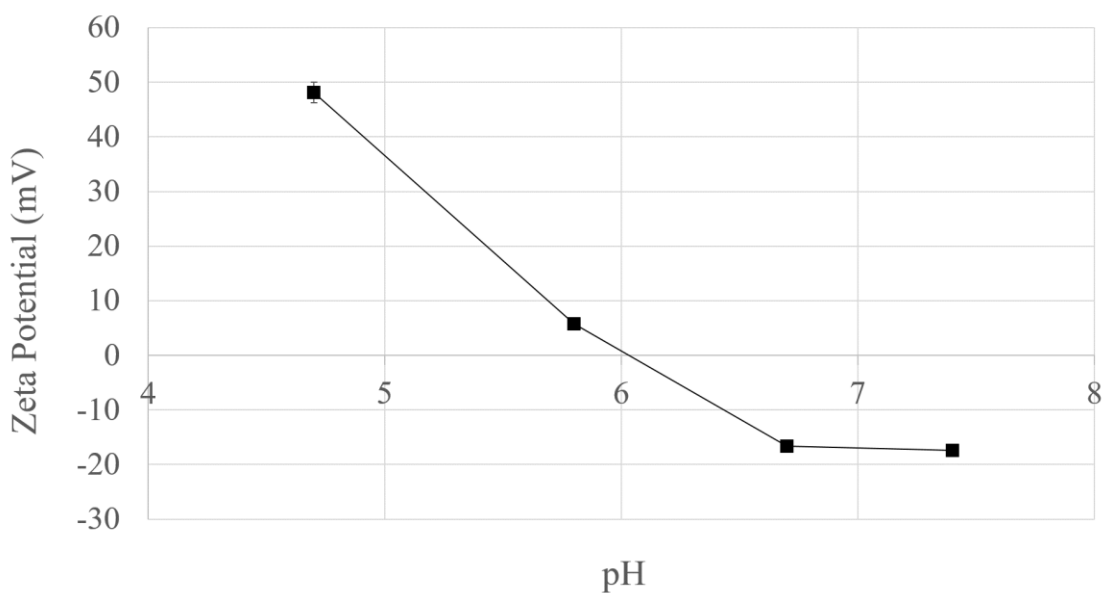


Figure 4. Zeta potential measurements of MSNP-amine at various pH levels.

Dynamic light scattering (DLS) was performed to show how the change in the charge of the particles affects the hydrodynamic size. DLS shows an increase in the hydrodynamic size of the MSNP-amine samples when the pH decreases. The size distribution for MSNP-amine particles dispersed in water at two different pH values is given in Figure 5.

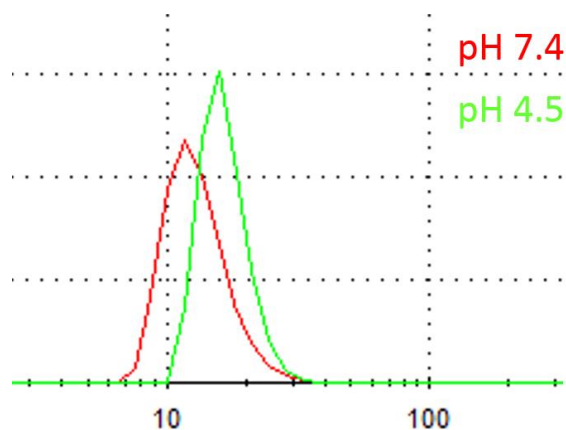


Figure 5. DLS number-average size distributions of MSNP-amine at pH 7.4 and 4.5.

The number-average size of the MSNP-amine increases from 13 nm to 17 nm when the pH is decreased from 7.4 to 4.5. This increase in size shows that the particles swell in an acidic environment. This is likely due to the protonation of the amine groups on the ligands. This protonation induces charge repulsion amongst the ligands, probably causing them to stretch out into the aqueous environment. However, the ligands are not long enough to produce a 4 nm size disparity among the samples of two different pH values by this effect alone. It is also likely that the hydrodynamic size is exaggerated in the pH 4.5 sample because the protonated ligands cause the water molecules to organize around the particles in an ordered fashion. The zeta potential and DLS reports are evidence that the MSNPs were successfully functionalized with (3-Trimethoxysilylpropyl)diethylenetriamine, and that there is indeed a pH response.

Controlled Release Results. After the MSNPs were loaded with rhodamine-B, the payload release was measured for both the MSNPs terminated with PEG-silane and the MSNP-amine samples. The release data for the PEG-silane is meant to act as a control to compare with the MSNP-amine. The release fraction

curves comparing the release of rhodamine-B from the PEG-silane MSNP drug delivery system at pH 4.5 and pH 7.4 are included in Figure 6. The fraction released was measured by dividing the maximum fluorescence intensity at each data point by the intensity at the final data point, when diffusion equilibrium is reached.

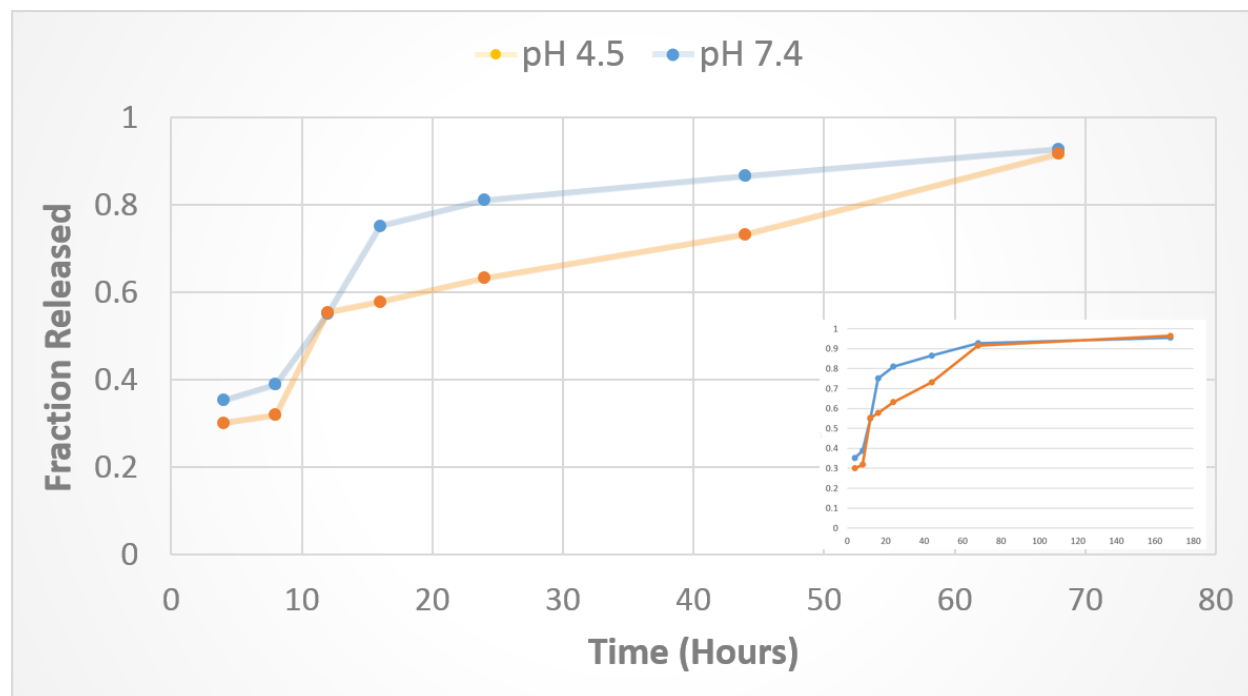


Figure 6: Fractional release curves of rhodamine-B from a 14.6 nm MSNP-PEG sample in pH 4.5 (red) and pH 7.4 (blue). The inset shows the same data with an additional measurement at 168 hours.

Release from PEG-terminated MSNP particles shows pH sensitivity, which was surprising. It is possible that at pH 4.5 the rhodamine-B amine groups became positively charged, and it became electrostatically attracted to the inherently negatively charged silica, limiting its diffusion out of the particle. This data is used as the control when evaluating the release of the pH-sensitive MSNP-amine samples.

The release data from the MSNP-amine is included in Figure 7. The data shows increased release rates from pH 4.5 and pH 6 relative to pH 7.4, which is the opposite trend as seen in the control data. This is evidence that the MSNP-amine samples show increased permeability at pH 6 and below, and that a pH-sensitive release is achieved.

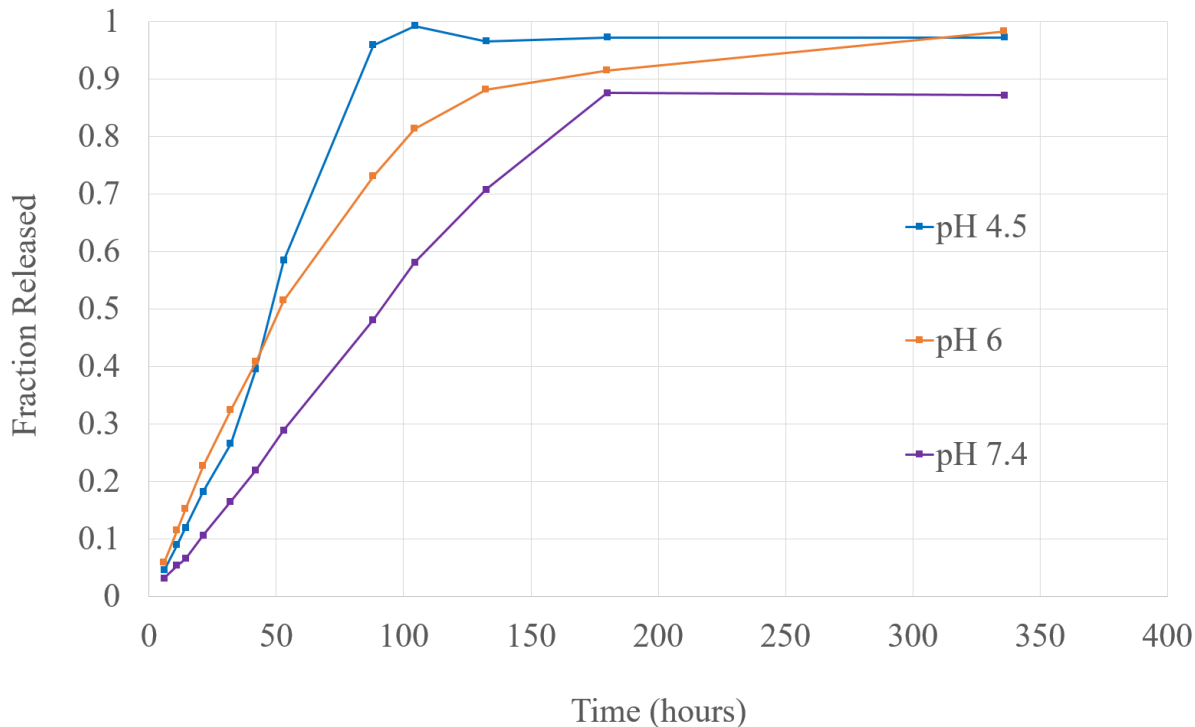


Figure 7: Fractional release curves of rhodamine-B from MSNP-amine at pH 4.6, 6, and 7.4.

In summary, a previously published procedure was successfully adapted to produce MSNP-amine samples that have permeability responsive to pH conditions. The new procedure used ammonium hydroxide to control the pH during synthesis, and substituted (3-Trimethoxysilylpropyl)diethylenetriamine for PEG-silane to functionalize the ligands with amine groups. At lysosomal pH (4.5), more of the rhodamine-B drug surrogate was released. Thus, with MSNP-amine particles as a drug delivery system, drug contents can be released more within the cells than without, leading to higher drug carrying efficiency. Additional benefits include minimized drug side effects and increased cost savings due to less drug wastage. This work confirms particle architectures similar to the ones used here might prove useful in the development of small-scale drug delivery nano-carriers for cancer therapy applications.

REFERENCES

1. Vallet-Regi, M.; Balas, F.; Acros, D. *Ang. Chem. Int. ed.* 46, 7548-7558. 2007.
2. You, J.; Almeda, D.; Ye, G.; Auguste, D. *J. Biol Eng.* 4: 15. 2010.
3. Anderson, R.; Mobley, D.; Blank, B. *J. of Urol.* 161.6. 1809-1812. 1999.
4. Ian Sample. *Materials World.* (10). 610-12.1999.
5. Hadaway, L. *Am. J. of Nurs.* 107 (8). 64-72. 2007.
6. Mather, L. *et al. Clinical Pharm. and Therap.* 17 (1). 21-30. 1975.
7. Allen, T.; Cullis, P. *Science.* 303 (5665). 1818-1822. 2004.
8. Schipper, M.; Gambhir, S.; *et al. Small.* 5 (1). 126-134. 2009.
9. Li, L.; Tang, F.; Liu, H.; Liu, T.; Hao, N.; Chen, D.; Teng, X.; He, J. *ACS Nano.* 4 (11). 6874-6882. 2010.
10. Jal, P.; Patel, S.; Mishra, B. *Talanta.* 62 (5). 1005-1028. 2004.
11. Burns, A.; Ow, H.; Wiesner, U. *Chem. Soc. Rev.* 35. 1028-1042. 2006.
12. Rosenholm, J.; Sahlgren, C.; Linden, M. *Nanoscale.* 2. 1870-1883. 2010.
13. Pan, L.; He, Q.; Liu, J.; Chen, Y.; Ma, M.; Zhang, L.; Shi, J. *J. Am. Chem. Soc.* 134 (13). 5722-5725. 2012.
14. Slowing, I.; Vivero-Escoto, J.; Wu, C.; Lin, V. *Adv. Drug Del. Rev.* 60 (11). 1278-1288. 2008.
15. Kim, J. *et al. Ang. Chemie. Int.* 47 (44). 8438-8441. 2008.
16. Tang, F.; Li, L.; Chen, D. *Adv. Mat.* 24 (12). 1504-1534. 2012.
17. Yang, P.; Gai, S.; Lin, J. *Chem. Soc. Rev.* 41. 3679-3698. 2012.
18. Asefa, T.; Tao, Z. *Chem. Res. Toxicol.* 25. 2265-2284. 2012.
19. Ma, K.; Werner-Zwanziger, U.; Zwanziger, J.; Wiesner, U. *Chem. Mater.* 25. 677-691. 2013.